Supporting Information

Evolution of active sites in Pt-based nanoalloy catalysts for oxidation of carbonaceous species by combined *in situ* infrared spectroscopy and total x-ray scattering

Valeri Petkov,[1,*] Yazan Maswadeh,[1] Aolin Lu [2], Shiyao Shan [2], Haval Kareem [2], Yinguang Zhao [2], Jin Luo [2], Chuan-Jian Zhong[2], Kevin Beyer [3] and Karena Chapman [3]

[1]Department of Physics, Central Michigan University, Mt. Pleasant, Michigan 48859, United States
[2]Department of Chemistry, State University of New York at Binghamton, Binghamton, New York 13902, USA
[3]X-ray Science Division, Advanced Photon Source, Argonne National Laboratory, Argonne, Illinois 60439, United States

Corresponding Author
* E-mail: petko1vg@cmich.edu

i) *Synthesis of Pt-Au and Pt-Au-Ni alloy nanoparticles (NPs)*

Binary Pt-Au and ternary Pt-Au-Ni NPs were synthesized by a facile one-pot synthesis method described in our earlier work.[1] In brief, Pt-Au-Ni NPs were synthesized by mixing $Pt(acac)_2$, $Ni(acac)_2$ and $HAuCl_4$ metal precursors in a pre-desired ratio with octadecene.1,2-hexadecanediol was added to the solution as a reducing agent, and oleic acid and oleylamine as capping agents. Temperature was increased fast (16 ºC/min) to 230 ºC with reflux for 1 h and the solution was cooled down to room temperature. Nanoparticles were precipitated out by adding ethanol and dispersed in hexane solvent for further use. Binary Pt-Au nanoparticles were synthesized by the same route this time using $Pt(acac)_2$ and $HAuCl_2$ metal precursors alone.

The as-synthesized NPs were deposited on fine titania powder and activated for catalytic applications by heating at 260 °C in 20 vol% O_2 for 30 min. Note that the activation is necessary to remove the organic molecules capping the NP surface. Besides, it stabilizes the NPs by annealing out likely atomic-level defects.[2,3] Hereafter, titania supported and post-synthesis processed Pt-Au and Pt-Au-Ni NPs are referred to as fresh NPs.

ii) *Determining the overall chemical composition, size and shape of Pt-Au and Pt-Au-Ni alloy NPs*

The overall chemical composition of fresh Pt-Au and Pt-Au-Ni alloy NPs was determined by inductively coupled plasma atomic emission spectroscopy (ICP-AES). Measurements were done on a Perkin Elmer 2000 DV ICP-AES instrument. Calibration was done against standards dissolved in the same acid matrix as the unknowns. Several batches of the unknowns were analysed thus ensuring < 2 % error in the overall chemical composition. Experimental data showed that the overall chemical composition of the NPs studied here is $Pt_{58}Au_{42}$, $Pt_{36}Au_9Ni_{55}$ and $Pt_{40}Au_{20}Ni_{40}$.

The NP size and shape were determined by Transmission Electron Microscopy (TEM) on a JEM-2200FS instrument operated at 200 kV. Exemplary TEM and high-resolution (HR)-TEM images of $Pt_{58}Au_{42}$, $Pt_{36}Au_9Ni_{55}$ and $Pt_{40}Au_{20}Ni_{40}$ NPs are shown in Figures S1 and S2, respectively. As can be seen in Figures, the NPs are approximately 6.8 (±1.0) nm in size and largely spherical in shape. Furthermore, as lattice fringes seen in the HR-TEM images show, the NPs possess a good degree of crystallinity. The NP size was also determined from the full width at half maximum of the Bragg-like peaks in the respective high-energy x-ray diffraction (HE-XRD)

patterns. Within the limits of the experimental accuracy, HE-XRD and TEM determined sizes of $Pt_{58}Au_{42}$, $Pt_{36}Au_9Ni_{55}$ and $Pt_{40}Au_{20}Ni_{40}$ NPs appeared about the same.

iii) Ex-situ studies on the CO oxidation activity of $Pt_{58}Au_{42}$, $Pt_{36}Au_9Ni_{55}$ and $Pt_{40}Au_{20}Ni_{40}$ NPs

The catalytic activity of fresh $Pt_{58}Au_{42}$, $Pt_{36}Au_9Ni_{55}$ and $Pt_{40}Au_{20}Ni_{40}$ alloy NPs for the CO oxidation reaction was determined on a custom-built system including a temperature-controlled reactor, gas flow controllers, an online gas chromatograph (Shimadzu GC 8A) equipped with 5A molecular sieve, Porapak Q packed columns and a thermal conductivity detector. Samples were loaded in a quartz microreactor tubing (inner diameter ~ 4 mm) and wrapped with quartz wool at both ends (length of the catalyst bed ~6 mm). The feeding gas CO (1 vol % CO plus 20 vol. % O_2 balanced by N_2) was injected continuously through the fixed catalyst's bed in the quartz microreactor at a flow rate of 20 mL/min. The residence time was about 0.2 s. Gas hourly space velocity (GHSV) in the system was around 16 000 h^{-1}. The CO conversion was determined by analyzing the composition of the tail gas effusing from the quartz microreactor using the online gas chromatograph. A representative set of CO conversion curves is shown in Figure S3. Data for the CO oxidation activity of the NPs are summarized in Table S3 in terms of the temperature, $T_{1/2}$, at which 50% of CO conversion (oxidation) is achieved. Values for the so-called turnover frequency (TOF), defined as TOF=Number of product (CO_2) molecules per the number of active sites at the NP surface per sec, are also given in the Table. Note that TOF values reported here are normalized against the total mass of Pt in the respective catalysts. Inspection of data in Table S3 shows that the CO oxidation activity of fresh NPs increases in the order $Pt_{40}Au_{20}Ni_{40} < Au_{42}Pt_{58} < Pt_{36}Au_9Ni_{55}$. Note that, regardless the type of the support, pure Au NPs with a size > 7-8 nm are hardly active as catalysts for CO oxidation (see Figure S4). On the other hand, pure Pt NPs in the 10nm-size size regime are active catalysts for CO oxidation reaction. However, under typical reaction conditions, the surface of Pt NPs may end up irreversibly covered with CO molecules thus becoming unreactive.[3] As shown here and elsewhere, binary and ternary nanoalloys of Pt with other noble and transition metals outperform pure Pt as catalysts for oxidation of carbonaceous species, including CO.[4-6]

iv) *In-situ high-energy x-ray diffraction (HE-XRD) combined with DRIFTS.*

Combined *in situ* high-energy x-ray diffraction (HE-XRD) and diffuse reflection infrared Fourier transform spectroscopy (DRIFTS) experiments were carried out using the DRIAD-X reaction cell at the beamline 11-ID-B at the Advanced Photon Source, Argonne.[7] The cell was mounted on a Bruker Vertex 80 spectrometer equipped with a Praying mantis-type optics. The optics allows DRIFTS measurements from a horizontal sample surface while the surface is probed with an x-ray beam. The ability to control the vertical size and position of the incoming x-ray beam ensured that the infrared (IR) and x-ray beams probed coinciding sample volumes. X-rays with energy of 86.70 keV (λ=0.1430 Å) were used and the scattered intensities were collected with a large area (amorphous Si) detector. At first, fresh $Pt_{58}Au_{42}$, $Pt_{36}Au_9Ni_{55}$ and $Pt_{40}Au_{20}Ni_{40}$ alloy NPs were heated at 130 ^oC in pure He atmosphere for 30 min to remove gas-phase species that may have been adsorbed on their surface before the *in situ* measurements. The NPs were then cooled down and exposed to CO oxidation reaction conditions (1% CO + 10 % O_2 in He) at 80 ^oC for 2 hours. Next, the NPs were reactivated by heating at 260 ^oC in oxygen-rich atmosphere (20% O_2 in He) for 30 min. The reactivated NPs were cooled down and exposed to CO oxidation reaction conditions (1 % CO + 10 % O_2 in He) at 80 ^oC for 2 more hours. DRIFTS and HE-XRD data were taken throughout the annealing in pure He and subsequent sequence of CO oxidation-reactivation-CO oxidation reactions in intervals of 10 min. For the DRIFTS measurements, spectra were collected in the range of 4000 to 400 cm^{-1} with a resolution of 2 cm^{-1}, averaging over 400-600 scans. At the very beginning of each step of the reaction sequence, background DRIFTS spectra were recorded and used for normalization and removing of spectral contributions of gas phase CO. Temporal evolution of DRIFTS spectra for $Pt_{58}Au_{42}$, $Pt_{36}Au_9Ni_{55}$ and $Pt_{40}Au_{20}Ni_{40}$ alloy NPs with the reaction conditions is shown in Figures 1a, 2a and 3a, respectively. For the HE-XRD measurements, data were collected in the range of 1 $Å^{-1}$ to 25 $Å^{-1}$ with a *q*-space resolution proven acceptable for atomic pair distribution function (PDF) studies.[7] Exemplary *in situ* HE-XRD patterns for $Pt_{58}Au_{42}$, $Pt_{36}Au_9Ni_{55}$ and $Pt_{40}Au_{20}Ni_{40}$ alloy NPs are shown in Figure S5. Atomic PDFs G(r) derived from the patterns are shown in Figure S6.

By definition, the PDF $G(r)=4\pi r(\rho(r)-\rho_o)$, where $\rho(r)$ and ρ_o are the local and average atomic number density of the materials under study, respectively. Hence, peaks in the experimental G(r)s shown in Figure S6 appear at distances between pairs of atoms (Pt, Au and/or Ni) within the studied

nanoalloy particles. The area under the peaks is proportional to the number of atomic pairs at those distances.[8] In particular, the first PDF peak reflects metal-to-metal atom bonding distances and coordination numbers. Note that G(r) oscillates about zero because, by definition, the average atomic number density, ρ_o, is subtracted from the local one, that is, from $\rho(r)$.

v) X-ray photoelectron spectroscopy (XPS) studies on fresh $Pt_{58}Au_{42}$, $Pt_{36}Au_9Ni_{55}$ and $Pt_{40}Au_{20}Ni_{40}$ alloy NPs

The relative percentage and electronic properties of near-surface Pt, Au and Ni atoms in fresh $Pt_{58}Au_{42}$, $Pt_{36}Au_9Ni_{55}$ and $Pt_{40}Au_{20}Ni_{40}$ alloy NPs were determined by XPS. Pure Pt NPs were also measured and used as a reference sample. Measurements were done on a Kratos AXIS Ultra DLD spectrometer equipped with a monochromatic Al source. The spectrometer was calibrated using C *1s* peak at 284.8 eV, Cu $2p_{3/2}$ peak at 932.7 eV and Au $4f_{7/2}$ peak at 84.0 eV as internal standards. The pass energy was fixed at 20 eV for the detailed scans. As an example, XPS Pt *4f* and Au *4f* spectra for $Pt_{36}Au_9Ni_{55}$ NPs are shown in Figures S9(a) and S9(b), respectively. The Pt *4f* spectrum for pure Pt NPs is also shown in Figure S9(a). As can be seen in Figure S9(a), the Pt $4f_{7/2}$ core-level peak position in $Pt_{36}Au_9Ni_{55}$ NPs is shifted by -0.7 eV with respect to the Pt $4f_{7/2}$ (71.0 eV) spectral line characteristic to bulk Pt . By contrast, the Pt $4f_{7/2}$ core-level peak position in pure Pt NPs is shifted by +0.8 eV with respect to the bulk value. The negative shift can be related to an increased overlap of the *d*-orbitals of nearby surface Pt atoms in $Pt_{36}Au_9Ni_{55}$ NPs due to compressive stress on the atoms. According to the *d*-band center theory, this would render Pt atoms in $Pt_{36}Au_9Ni_{55}$ NPs less reactive as compared to atoms in corresponding pure Pt NPs. As can be seen in Figure S9(b), the Au $4f_{7/2}$ core-level peak position in $Pt_{36}Au_9Ni_{55}$ NPs is shifted by -1.6 eV with respect to the Au $4f_{7/2}$ (84.0 eV) spectral line characteristic to bulk Au. Concurrent negative shifts of Pt $4f_{7/2}$ and Au $4f_{7/2}$ core-level peak positions in Pt-Au mixtures have been attributed to alloying of Pt and Au atoms in the mixtures.[9] Notably, Pt $4f_{7/2}$ and Au $4f_{7/2}$ core-level peak positions in $Pt_{58}Au_{42}$ and $Pt_{40}Au_{20}Ni_{40}$ NPs also appear shifted to lower energy as compared to the bulk values (see Table S1). Overall, XPS data indicate the presence of strong interactions between noble metal atoms forming the fresh nanoalloy particles studied here, including changes in the electronic structure of the atoms. Note that the shift in the binding energy of Ni atoms was difficult to determine because of the severe overlap of contributions from Ni^0, Ni^{2+} and Ni^{3+} species to the XPS Ni *2p* spectra for the NPs (e.g. see Figure S9c).

The near-surface composition of the NPs was determined from the experimental XPS spectra. Results are summarized in Table S2 together with data for the bulk composition of the NPs obtained by ICP-AES. Analysis of the data in the Table indicates that, within the limits of the experimental accuracy, fresh NPs studied here are near random alloys.

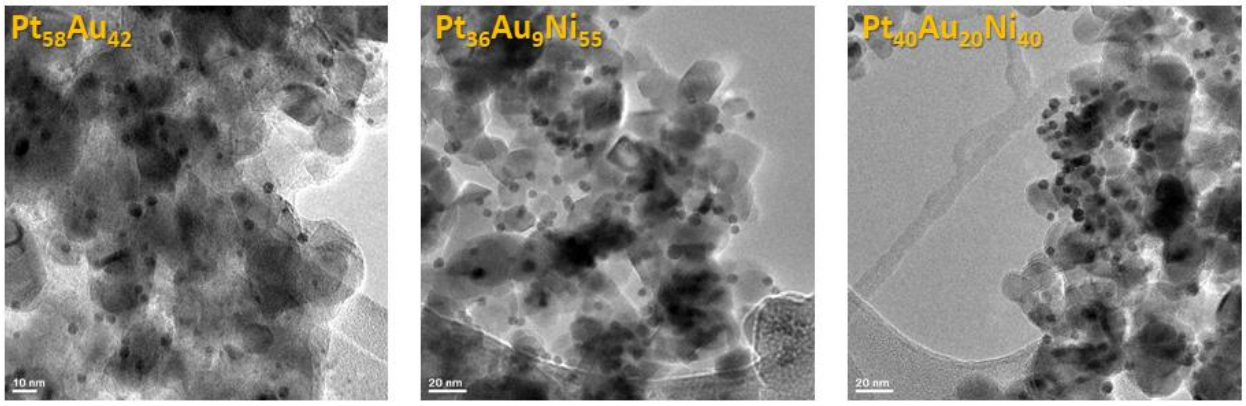

Figure S1. Representative TEM images for $Pt_{58}Au_{42}$, $Pt_{36}Au_9Ni_{55}$ and $Pt_{40}Au_{20}Ni_{40}$ alloy NPs. The NPs appear with an average size of 6.8 (±1.0) nm, spherical in shape and well dispersed on the carbon support. Note, the "±" deviation from the average NP size is the half width at full maximum of a gaussian-like distribution of sizes extracted from populations of several hundred NPs sampled by different TEM images.

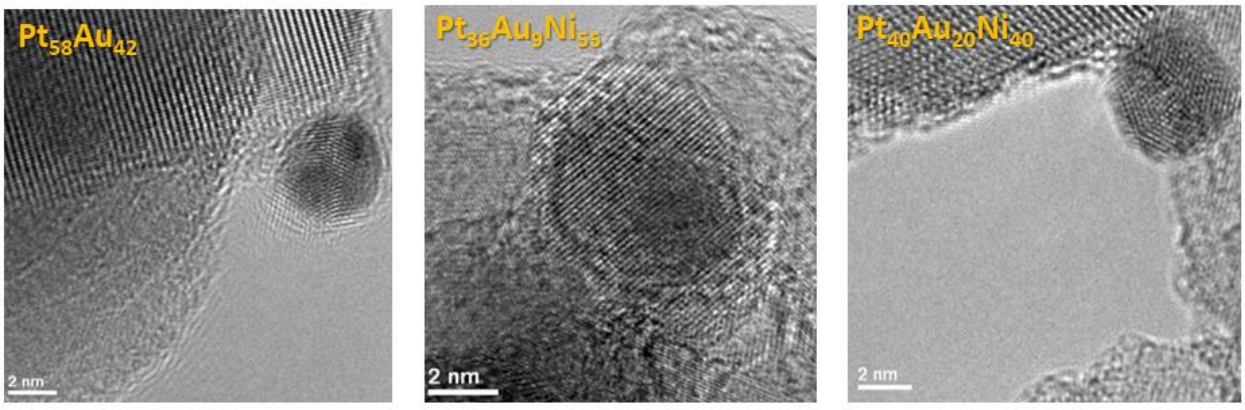

Figure S2. Representative HR-TEM images for $Pt_{58}Au_{42}$, $Pt_{36}Au_9Ni_{55}$ and $Pt_{40}Au_{20}Ni_{40}$ alloy NPs. The NPs possess a good degree of crystallinity as indicated by the lattice fringes seen in the images.

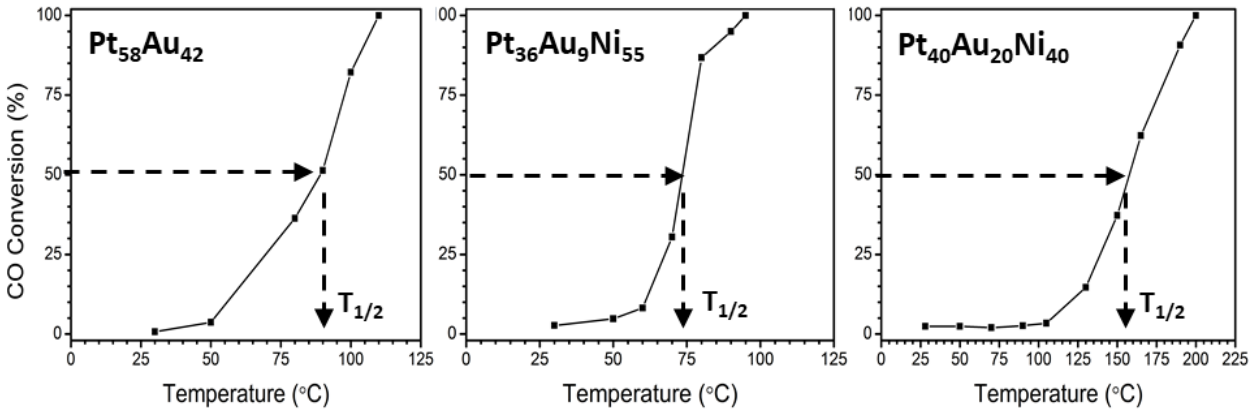

Figure S3. CO conversion rate over fresh $Pt_{58}Au_{42}$, $Pt_{36}Au_9Ni_{55}$ and $Pt_{40}Au_{20}Ni_{20}$ nanoalloy catalysts. Broken lines show the so-called $T_{1/2}$ that is the temperature at which 50 % conversion of CO to CO_2 is achieved. Values for $T_{1/2}$ are summarized in Table S3.

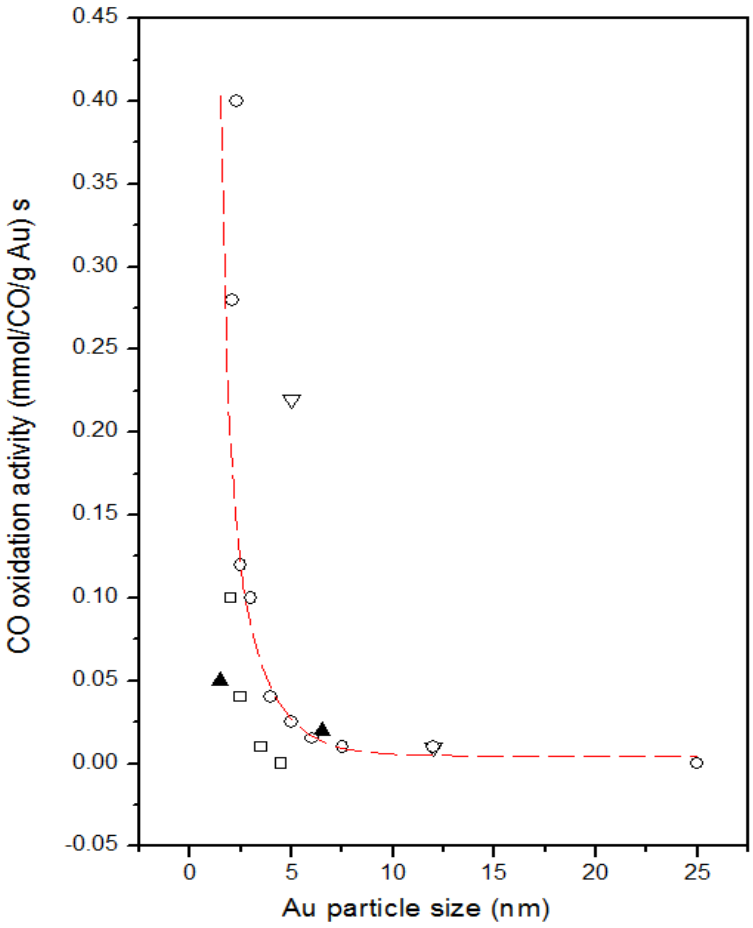

Figure S4: Reported catalytic activities of Au NPs for CO oxidation as a function of Au particle size. Data are taken at 0 ºC. The supports are indicated as follows: down triangle – Fe_2O_3, square – Al_2O_3, up triangles – SiO_2 and circles – TiO_2. The broken line fitted to the data scales with the calculated number of atoms located at corners (coordination number of six) of NPs with the shape of a truncated octahedron. Adapted with permission from reference (10). Copyright (2007) Elsevier).

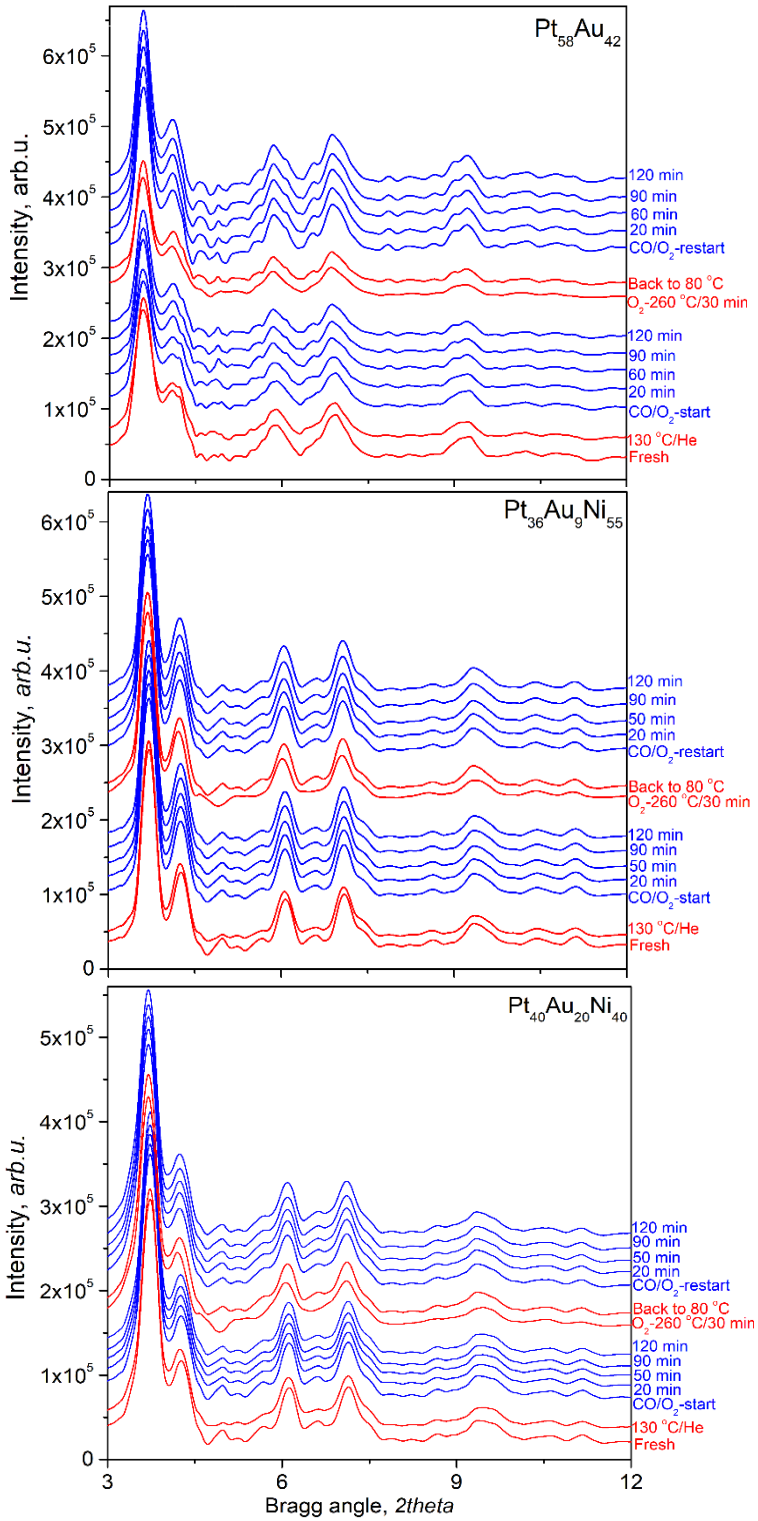

Figure S5. Exemplary *in situ* HE-XRD patterns for $Pt_{58}Au_{42}$, $Pt_{36}Au_9Ni_{55}$ and $Pt_{40}Au_{20}Ni_{40}$ alloy NPs. The thermo-chemical conditions at which the patterns are obtained are given for each data set (see text on the right hand side of the graphs). Note that only the low-angle part of the patterns is shown to reveal better fine features of the Bragg-like peaks in the patterns.

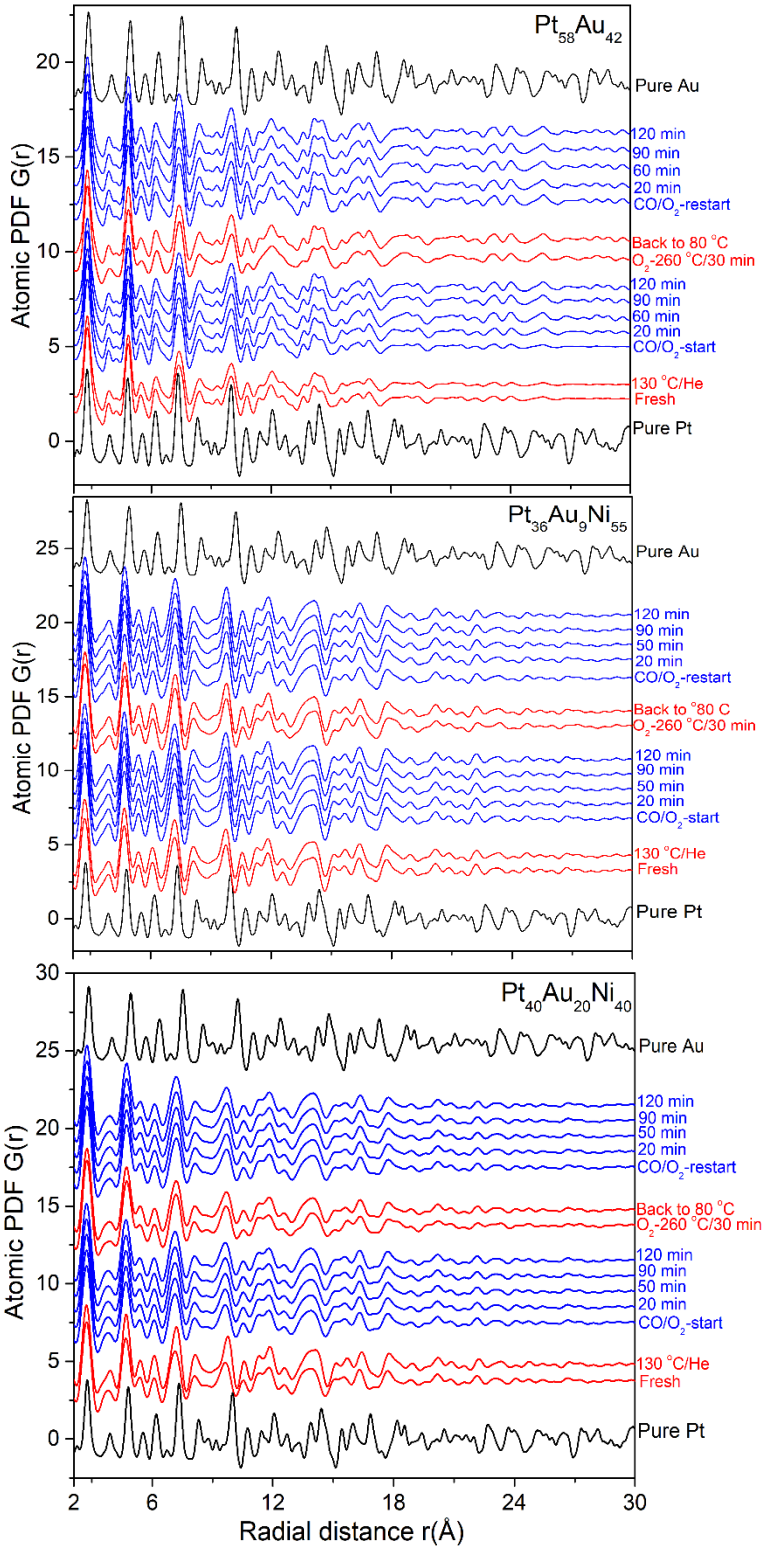

Figure S6. *In situ* atomic PDFs for $Pt_{58}Au_{42}$, $Pt_{36}Au_9Ni_{55}$ and $Pt_{40}Au_{20}Ni_{40}$ alloy NPs. The PDFs are derived from the HE-XRD patterns shown in Figure S5.

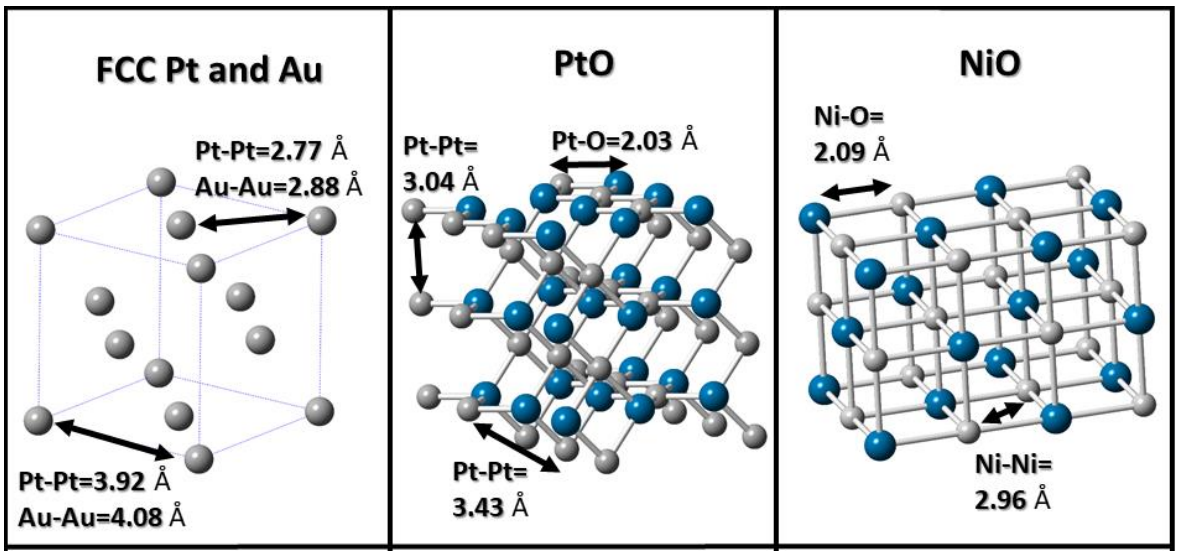

Figure S7. Characteristic metal-metal and metal-oxygen first neighbor distances in pure fcc Pt, fcc Au, tetragonal PtO and cubic NiO.[11] Metal atoms are in gray and oxygen atoms are in blue.

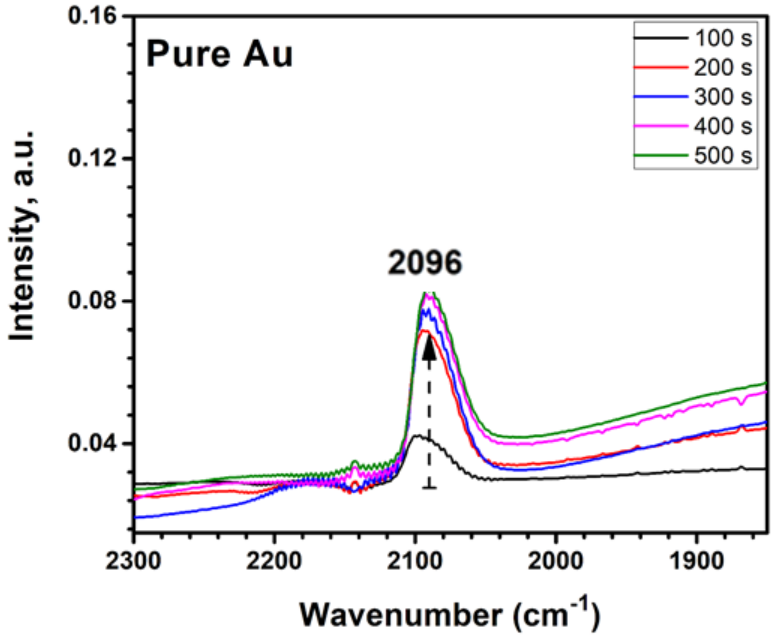

Figure S8. DRIFTS spectra for titania supported pure Au NPs exposed to CO oxidation conditions. The spectra exhibit a somewhat asymmetric band centered at about 2096 cm^{-1}. The band can be attributed to CO molecules that are linearly adsorbed (atop) on planar (e.g. terraces) surface Au sites.[6,12]

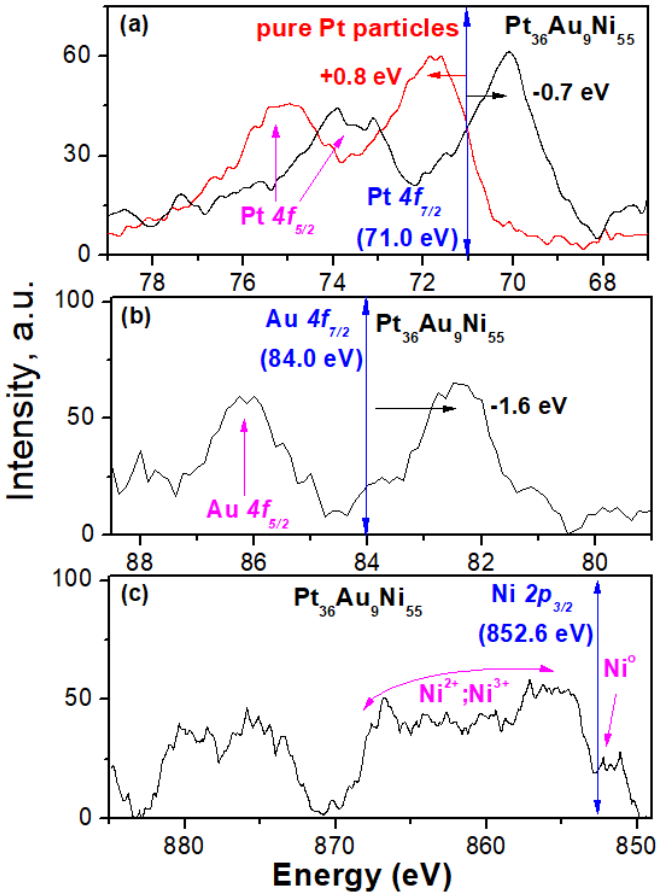

Figure S9. *(a)* Typical XPS Pt $4f_{7/2}$ spectrum for fresh $Pt_{36}Au_9Ni_{55}$ (black line) and pure Pt (red line) NPs. The negative (-0.7 eV; follow the black arrow) and positive (+0.8 eV; follow the red arrow) shift of the binding energy of Pt atoms in the respective NPs is evaluated with respect to the Pt $4f_{7/2}$ spectral line (71.0 eV; see the vertical blue line) characteristic for bulk Pt. Note that the Pt $4f_{5/2}$ spectral line is also seen at a higher binding energy (magenta arrows). The Pt $4f_{7/2}$ and $4f_{5/2}$ spectral lines are rather broad and asymmetric in shape, indicating the presence of a significant local structural disorder and/or partial oxidation of Pt atoms in the respective NPs. *(b)* Typical XPS Au $4f_{7/2}$ spectrum for $Pt_{36}Au_9Ni_{55}$ (blue line) NPs. The negative (-1.6 eV; follow the black arrow) shift of the binding energy of Au atoms in the NPs is evaluated with respect to the Au $4f_{7/2}$ spectral line (84.0 eV; see the vertical blue line) characteristic for bulk Au. Note that the Au $4f_{5/2}$ spectral line is also seen at a higher binding energy (magenta arrow). The Au $4f_{7/2}$ and $4f_{5/2}$ spectral lines are rather broad but well resolved and nearly symmetric in shape, indicating that the Au species in the NPs are unlikely to be oxidized. *(c)* Typical XPS Ni $2p_{3/2}$ spectrum for $Pt_{36}Au_9Ni_{55}$ (black line) NPs. The Ni $2p_{3/2}$ spectral line (853.0; see the vertical blue line) characteristic for bulk Ni is also shown. The small hump at about 852 eV (magenta arrow) can be attributed to Ni^o metallic species. The broad features at higher binding energies (magenta arc) can be attributed to oxidized Ni species in the NPs, in particular Ni^{2+} and Ni^{3+} species.[13,14]

Table S1.Shift in the Pt $4f_{7/2}$, Au $4f_{7/2}$ and Ni $2p_{3/2}$ spectral lines for fresh $Au_{42}Pt_{58}$, $Pt_{36}Au_9Ni_{55}$ and $Pt_{40}Au_{20}Ni_{40}$ nanoalloy catalysts as determined by XPS experiments. Note that the Ni $2p_{3/2}$ line for the NPs appears as a superposition of heavily overlapping lines characteristic to Ni^o, Ni^{2+} and Ni^{3+} species. Hence, the shift in its position with respect to the bulk value is difficult to determine accurately.

Catalysts	**Shift in Pt $4f_{7/2}$ line**	**Shift in Au $4f_{7/2}$ line**	**Shift in Ni $2p_{3/2}$ line**
$Pt_{36}Au_9Ni_{55}$	-0.7 eV	-1.6 eV	Ambiguous
$Pt_{40}Au_{20}Ni_{40}$	-0.5 eV	-1.1 eV	Ambiguous
$Au_{42}Pt_{58}$	-0.2 eV	-0.3 eV	N/A

Table S2.Bulk vs surface composition for fresh $Au_{42}Pt_{58}$, $Pt_{36}Au_9Ni_{55}$ and $Pt_{40}Au_{20}Ni_{40}$ nanoalloy catalyst as determined by ICP-AES and XPS experiments, respectively. Note that the XPS is indeed sensitive to the near surface region of the NPs and not the top surface layer of the NPs alone. Nevertheless, XPS data may reveal large differences in the chemistry of the NP "surface" and "interior". Data shows that the fresh NPs studied here can be considered as near random alloys.

Bulk (ICP-AES)	Surface (XPS)
$Pt_{36}Au_9Ni_{55}$	$Pt_{39}Au_7Ni_{54}$
$Pt_{40}Au_{20}Ni_{40}$	$Pt_{44}Au_{22}Ni_{34}$
$Au_{42}Pt_{58}$	$Au_{48}Pt_{52}$

Table S3.Summary of $T_{1/2}$ and TOF values (at 80 ^oC) for fresh $Au_{42}Pt_{58}$, $Pt_{36}Au_9Ni_{55}$ and $Pt_{40}Au_{20}Ni_{40}$ nanoalloy catalyst for CO oxidation reaction. Data shows that the activity of the catalysts increases in the order $Pt_{40}Au_{20}Ni_{40} < Au_{42}Pt_{58} < Pt_{36}Au_9Ni_{55}$.

Catalysts	TOF (x 10^{-2} s^{-1})	$T_{1/2}$ (^oC)
$Pt_{36}Au_9Ni_{55}$	5.34	75
$Pt_{40}Au_{20}Ni_{40}$	0.032	160
$Au_{42}Pt_{58}$	2.49	90

References (SI):

(S1) Yang, L.; Shan, Sh.; Loukrakpam, R.; Petkov, P.; Ren, Y.; Wanjala, B. N.; Engelhard, M. H.; Luo, J.; Yin, J.; Chen, Y.; Zhong, Ch.-J. Role of Support−Nanoalloy Interactions in the Atomic-Scale Structural and Chemical Ordering for Tuning Catalytic Sites. *J. Am. Chem. Soc.* **2012,** *134***,** 15048-15060.

(S2) Wang, C.; Vliet, D.; More, K. L.; Zaluzec, N. J.; Peng, S.; Sun, S.; Daimon, H.; Wang, C.; Greeley, J.; Pearson, J.; Paulikas, A. P.; Karapetrov, G.; Strmcnik, D.; Markovic N. M.; Stamenkovic, V. R. Multimetallic Au/$FePt_3$ Nanoparticles as Highly Durable Electrocatalyst. *Nano Lett*. **2011**, *11*, 919-926.

(S3) Cheah, S. K.; Bernardet, V. P.; Franco, A. A.; Lemaire, O.; Gelin, P. Structural and Surface Coverage Effects on CO Oxidation Reaction over Carbon-Supported Pt Nanoparticles Studied by Quadrupole Mass Spectrometry and Diffuse Reflectance FTIR spectroscopy. *PhysChemChemPhys* **2016**, *18*, 15278-1528.

(S4) Shan, S.; Petkov, V.; Yang, L.; Mott, D.; Wanjala, B. BN.; Cai, F.; Chen, B. H.; Luo, J.; Zhong, Ch.-J. Oxophilicity and Structural Integrity in Maneuvering Surface Oxygenated Species on Nanoalloys for CO Oxidation. *ACS Catalysis* **2013**, *13*, 3075-3085.

(S5) Cuenya, B. R.; Behafarid, F. Nanocatalysis: Size- and Shape-Dependent Chemisorption and Catalytic Reactivity. *Surf. Sci. Rep*. **2015**, *70*, 135-187.

(S6) Mott, D.; Luo, J.; Njoky, P. N.; Lin, Y.; Wang, L.; Zhong, Ch.-J. Synergistic Activity of Gold-Platinum Alloy Nanoparticle Catalysts. *Catal. Today* **2007**, *122*, 378-385.

(S7) Beyer, B. H.; Zhao, H.; Borkiewicz, O. J.; Newton, M. A.; Chupas, P. J.; Chapman, K. W. Simultaneous Diffuse Reflection Infrared Spectroscopy and X-ray Pair Distribution Function Measurements. *J. Appl. Crystallogr*. **2014**, *47*, 95-101.

(S8) Petkov, V. Nanostructure by High-Energy X-ray Diffraction. *Materials Today* **2008**, *11*, 28-38.

(S9) Ge, X.; Yan, X.; Wang, R.; Tang, F.; Ding Y. Tailoring the Structure and Property of Pt-Decorated Nanoporous Gold by Thermal Annealing. *J. Phys. Chem. C* **2009**, *113*, 7379-7384.

(S10) Hvolbaek, B.; Janssens, T. V. W.; Clausen, B. S.; Falsig, H.; Christensen, C. H.; Norskov, J. K. Catalytic Activity of Au Nanoparticles. *Nanotoday* **2007**, *2,* 14-18.

(S11) W. J. Moore, W. J.; Pauling, L. The Crystal Structures of the Tetragonal Monoxides of Lead, Tin, Palladium, and Platinum. *J. Am. Chem. Soc.* **1941**, *63*, 1392-1394.

(S12) Mihut, C.; Descorme, D.; Duprez, D.; Amiridis, M. D. Kinetic and Spectroscopic Characterization of Cluster-Derived Supported Pt–Au Catalysts. *J. Catal.* **2002**, *212*, 125-135.

(S13) Parkinson, C. R.; Walker, M.; McConville, C. F. Reaction of Atomic Oxygen with a Pt(111) Surface: Chemical and Structural Determination Using XPS, CAICISS and LEED. *Surf. Sci*. **2003**, *545*, 19-33.

(S14) Grosvenor, A. P.; Biesinger, M. C.; Smart, R. St. C.; McIntyre, N. S.; New Interpretations of XPS Spectra of Nickel Metal and Oxides. *Surf. Sci*. **2006**, *600*, 1771-1779.